RSC Advances

PAPER

View Article Online
View Journal | View Issue

Cite this: *RSC Adv.*, 2026, **16**, 22672

Evaluation of the electronic, optical, thermoelectrical and magnetic properties of manganite perovskites *via* DFT calculations and critical exponent analysis

Line Karoui, *[a] Ala Eddin Mabrouki,[b] Taoufik Mnasri, [a] Anna Bajorek [c] and Mourad Smari [b]

Received 26th February 2026
Accepted 14th April 2026

DOI: 10.1039/d6ra01703g

rsc.li/rsc-advances

Samples of $La_{0.8}Sr_{0.2}Mn_{0.8}Co_{0.2}O_3$ were synthesized using the sol–gel method at different gelation temperatures to study their electronic, optical, thermoelectric and magnetic properties. Electronic structure calculations for the spin-down configuration reveal a p-type semiconducting behaviour with an indirect band gap of 3.44 eV, while the spin-up configuration exhibited metallic behaviour. Density of states analysis shows a clear spin asymmetry and significant Mn–Co–O hybridization near the Fermi level. The optical results present a high static dielectric constant and strong ultraviolet absorption below 300 nm, with a derived band gap of 3.44 eV, consistent with band structure analysis. The power factor increased steadily with temperature, suggesting suitability for thermoelectric use at high temperatures. Magnetic characterization using modified Arrott plots, Kouvel–Fisher analysis and scaling hypothesis enables determination of the critical exponent, suggesting short-range ferromagnetic interactions or mixed-range magnetic ordering depending on the gelation temperature.

1 Introduction

Perovskite oxides of the type $LaMO_3$ (where M = Mn or Co) exhibit a wide range of intriguing properties driven by the strong coupling between charge, spin, orbital and lattice degrees of freedom. The parent compound, $LaMnO_3$, is known for its antiferromagnetic behaviour due to the cooperative Jahn–Teller distortion and orbital ordering of Mn^{3+} ions.[1]

Partial substitution of La^{3+} with Sr^{2+} introduces Mn^{4+} species, enhancing double-exchange interactions and leading to a transition towards ferromagnetic to metallic states.[2,3] In contrast, $LaCoO_3$ shows a series of spin-state transitions in Co^{3+} ions, influenced by temperature and doping, as the system varies from low-spin to intermediate- or high-spin configurations.[4,5]

The composition $La_{0.8}Sr_{0.2}Mn_{0.8}Co_{0.2}O_3$ (LSMCO) combines both Mn and Co at the B site and Sr at the A site, allowing simultaneous tuning of electronic structure and magnetic interactions. The complexity arising from the Mn–Co interactions and mixed valence states makes this system particularly attractive for exploring correlated electronic and magnetic phenomena. Recent work has shown that even synthesis parameters, such as the gelation temperature, can significantly influence the magnetic and magnetocaloric properties of similar perovskites, indicating their sensitivity to subtle structural variations.[6]

From a theoretical perspective, density functional theory (DFT), especially when enhanced with Hubbard corrections or hybrid functionals, has proven effective in describing the electronic structure of these materials. Earlier investigations on $LaMnO_3$ have demonstrated how orbital ordering and lattice distortions affect magnetic ordering,[7] while investigations on $LaCoO_3$ have underlined the importance of selecting appropriate exchange correlation functionals to capture spin-state energetics accurately.[8]

The interplay between Mn and Co in systems such as LSMCO is expected to introduce additional electronic complexity, including strong hybridization effects and spin polarization near the Fermi level, which can be effectively explored through DFT + U approaches.[9,10]

In order to identify the predominant interaction mechanisms, it is imperative to perform a comprehensive analysis of the magnetic transition. This is typically done by extracting critical exponents (α, β, and γ) from magnetization measurements near the Curie temperature. These parameters allow classification of the transition within a universality class, reflecting whether the behaviour is closer to a mean field, 3D Ising, 3D Heisenberg or tri-critical mean field model. Previous

[a]*Laboratory of Technology, Energy and Innovative Materials, TEMI, Faculty of Sciences of Gafsa, University of Gafsa, 2112, Tunisia. E-mail: linekaroui5@gmail.com*
[b]*Laboratory of Applied Physics, Faculty of Sciences of Sfax, University of Sfax, B. P. 1171, 3000 Sfax, Tunisia*
[c]*A.Chelkowski Institute of Physics, University of Silesia in Katowice, 75 Pulku Piechoty 1, 41-500 Chorzow, Poland*

studies on related compounds, such as $La_{0.88}Sr_{0.12}MnO_3$ (ref 11) and $La_{0.8}Ca_{0.2}Mn_{1-x}Co_xO_3$,[12] have shown how cation substitution and local disorder can shift the critical behaviour and even lead to tri-critical phenomena.[13,14]

In our previous work, the effect of the gelation temperature on the structural, magnetic and magnetocaloric properties of $La_{0.8}Sr_{0.2}Mn_{0.8}Co_{0.2}O_3$ was systematically investigated, revealing a strong dependence of these properties on synthesis conditions.[6] However, the microscopic origin of these variations, especially from an electronic structure perspective, remains to be fully elucidated.

To bridge this gap, in this present study, we investigate the electronic and magnetic properties of $La_{0.8}Sr_{0.2}Mn_{0.8}Co_{0.2}O_3$ prepared at different gelation temperatures. Spin-polarized DFT calculations are used to model the electronic structure and evaluate the optical and thermoelectrical properties, while the nature of the magnetic phase transition is analyzed through critical exponent analysis, building on the magnetic characterization previously reported for the same compound.[6]

2 Experimental

Three $La_{0.8}Sr_{0.2}Mn_{0.8}Co_{0.2}O_3$ compounds, designated LS1, LS2 and LS3, were prepared using a sol–gel method. Appropriate stoichiometric amounts of $La(NO_3)_3\cdot 6H_2O$, $Sr(NO_3)_2$, MnO_2, and hydrated cobalt carbonate (CH_2CoO_4) were used as starting materials. Citric acid was added as a chelating agent to ensure the homogeneity of the solution.

The precursors were dissolved in distilled water under continuous stirring until a homogeneous solution was obtained. Upon heating, the solution transformed into a gel, which further evolved into a resin. The gel formation temperature was fixed at 70 °C, 90 °C and 300 °C, respectively, during the preparation process, as indicated in our previous work.[6]

The obtained gels were heated at 300 °C to remove residual organic matter and yield a powder. The powders were then ground for 30 minutes to improve the homogeneity, followed by calcination at 600 °C for 24 hours in air. After a second grinding step, a final sintering was carried out at 900 °C for 24 hours in air to ensure phase formation and crystallinity.

The crystal structures of the obtained samples LS1, LS2 and LS3 were determined with an X-ray diffractometer using a characteristic wavelength of copper $\lambda(\mathrm{Cu}) = 1.54056$ Å, at room temperature. The diffractograms obtained show that samples LS1, LS2 and LS3 crystallize in a rhombohedral structure with space group $R\bar{3}C$ and do not exhibit any secondary phase.

3 Computational details

Density functional theory describes the electronic structure of a material in its ground state at zero temperature. As the LS1, LS2 and LS3 samples correspond to the same compound, $La_{0.8}Sr_{0.2}Mn_{0.8}Co_{0.2}O_3$, and crystallize in the same structural phase, a single representative DFT calculation is sufficient.

For a reliable numerical study of $La_{0.8}Sr_{0.2}Mn_{0.8}Co_{0.2}O_3$ manganite, structural parameters obtained from the X-ray diffraction refinement were used. A $1 \times 1 \times 5$ supercell containing 24 La atoms, 6 Sr atoms, 24 Mn atoms, 6 Co atoms, and 90 O atoms was adopted. The calculations were performed using the full potential linearized augmented plane wave (FP-LAPW) method implemented in the Win2k software.

The exchange-correlation effect was treated within the Generalized Gradient Approximation (GGA) using the Perdew–Burke–Ernzerhof (PBE) functional. The nature of the localized Mn and Co d electrons was addressed by applying an on-site Coulomb correction using the Hubbard U approach, with an effective value of $U_{\mathrm{eff}} = 4.0$ eV and 5.5 eV for Mn and Co, respectively.

A ferromagnetic ordering between the Mn and Co moments was adopted. Calculations were performed using 2000 k-points for Brillouin zone integration and an $Rk_{\max}$ value of 7, where R is the smallest muffin-tin radius, and $k_{\max}$ is the plane-wave cutoff.

The self-consistent field (SCF) calculations were stabilized and considered converged when the charge difference between iterations was less than $0.001e^-$ and the total energy difference was below 10^{-5} eV. The muffin-tin radii 'R_{mt}' values were set to 2.38, 2.20, 1.80, 1.80 and 1.61 a.u for La, Sr, Mn, Co and O atoms, respectively.

The thermoelectric properties of $La_{0.8}Sr_{0.2}Mn_{0.8}Co_{0.2}O_3$ were investigated in the temperature range from 20 K to 1200 K using Boltzmann transport theory as implemented in the BoltzTrap code within the constant relaxation time approximation.[15] The calculated transport coefficients correspond to σ/τ and $\kappa_{\mathrm{tot}}/\tau$, where τ is assumed to be constant.

4 Results and discussion

4.1 Electronic structure

Fig. 1 depicts the band structure of the $La_{0.8}Sr_{0.2}Mn_{0.8}Co_{0.2}O_3$ compound in both spin-up and spin-down configurations. According to the spin-down configuration, the $La_{0.8}Sr_{0.2}Mn_{0.8}$-$Co_{0.2}O_3$ sample exhibits a p-type semiconducting behaviour with an indirect energy gap $E_g = 3.44$ eV. However, in the spin-up configuration, where there is an overlap between the valence and conduction bands, it exhibits metallic properties. The presence of these features indicates the semi-metallic nature of the sample.[16]

To understand the mobility and behaviour of the holes and electrons in the compound, their effective masses were calculated using the following expression:[17]

$$\frac{1}{m^*} = \frac{1}{\hbar^2} \times \frac{d^2E}{\mathrm{d}k^2} \quad (1)$$

The thermal velocities were derived from static physics by the equation below:[17]

$$V_{\mathrm{th}} = \sqrt{\frac{3K_{\mathrm{B}}T}{m^*}} \quad (2)$$

The electron and hole densities were obtained from the following equations:[17]

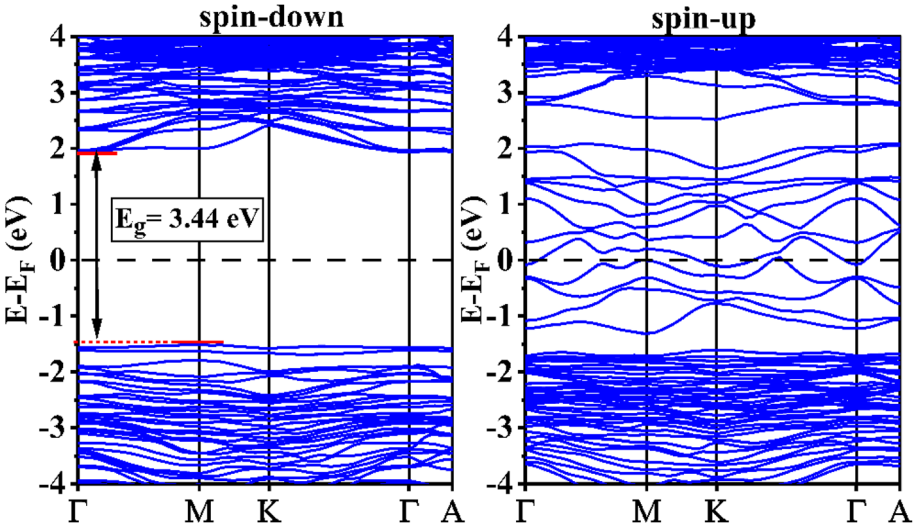

Fig. 1 Calculated electronic band structures of the $La_{0.8}Sr_{0.2}Mn_{0.8}Co_{0.2}O_3$ compound for both spin-down and spin-up states.

$$n = 2\frac{(2\pi m_e^* K_B T)^{3/2}}{h^3}\exp\left(-\frac{E_C - E_F}{K_B T}\right) \quad (3)$$

$$p = 2\frac{(2\pi m_h^* K_B T)^{3/2}}{h^3}\exp\left(-\frac{E_V - E_F}{K_B T}\right) \quad (4)$$

The results of effective masses, thermal velocities, and densities of electrons and holes are summarized in Table 1.

The significantly higher mass of holes suggests lower hole mobility compared to electrons, and the corresponding thermal velocity values confirm that electrons are indeed more mobile. However, the calculated carrier concentrations indicate p-type character as the hole density exceeds the electron density.

Fig. 2 shows the total density of states of the sample $La_{0.8}Sr_{0.2}Mn_{0.8}Co_{0.2}O_3$. An asymmetry between the density of states for spin-up and spin-down configurations is evident, indicating the ferromagnetic behaviour of the sample, which has already been determined experimentally.[6]

The partial density of states (PDOS) of each atom is presented in Fig. 3 to provide a better understanding of the electronic structure of the sample. As shown in Fig. 3, Mn d and Co d are the main contributors to the electronic structure in both spin-up and spin-down configurations around the Fermi energy. PDOS plots near the Fermi level for the spin-up configuration show strong hybridization between Mn d, Co d and O p orbitals. The metallic behaviour of the sample is attributed to this hybridization, which aligns with previous studies on transition-metal perovskites, where the electronic structure is largely governed by the interaction between transition-metal d-states and oxygen p-states.[6,18] In manganite-based systems, the MnO_6 octahedra undergo Jahn–Teller distortions,[1] leading to the splitting of the 3d orbitals into t_{2g} and e_g states.[19] The resulting high density of hybridized e_g-O_{2p} states near E_F facilitates electron hopping between neighboring Mn and Co sites through the oxygen bridge. This behaviour is consistent with a double-exchange-like mechanism, in which the delocalization of e_g electrons contributes to the alignment of localized spins and thus influences the magnetic order of the system.[6,20]

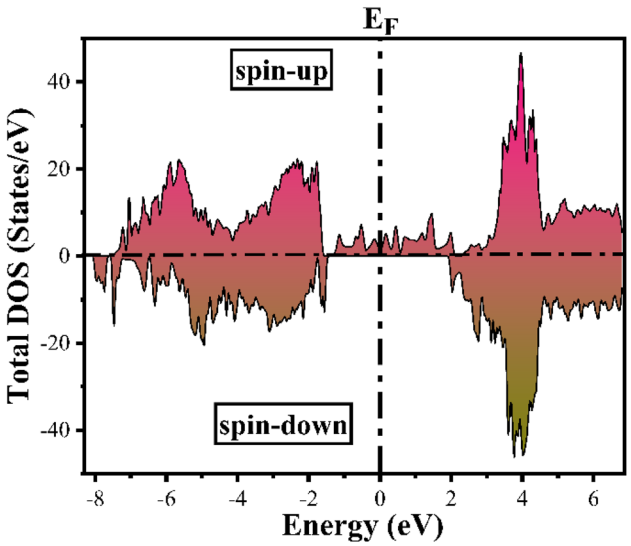

Fig. 2 Calculated total density of states for $La_{0.8}Sr_{0.2}Mn_{0.8}Co_{0.2}O_3$ in both spin-up and spin-down states.

Table 1 Electronic parameters obtained *via* DFT calculations for $La_{0.8}Sr_{0.2}Mn_{0.8}Co_{0.2}O_3$

E_g (Ev)	$m_e^*(m_e)$	$m_h^*(m_e)$	V_{th}^e(m s^{-1})	V_{th}^h (m s^{-1})	N_C (m^{-3})	N_V (m^{-3})	n (m^{-3})	p (m^{-3})
3.44	0.484	1.679	1.6787×10^5	9.0156×10^4	8.4236×10^{24}	5.4382×10^{25}	1.0948×10^{-4}	7.0844×10^{-4}

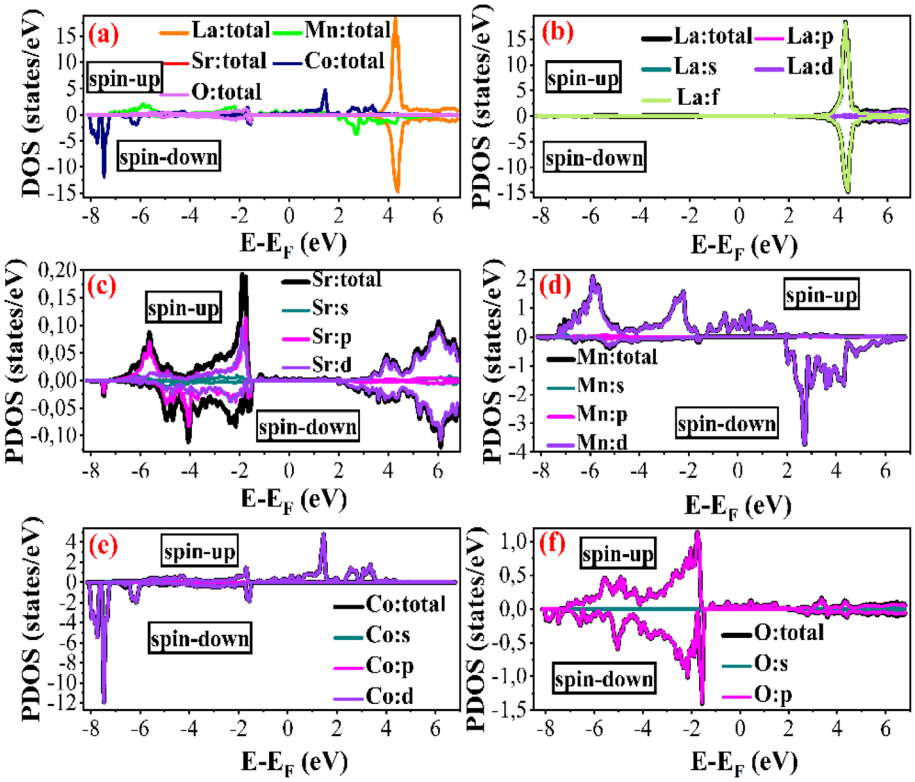

Fig. 3 (a) Total density of states (DOS) of $La_{0.8}Sr_{0.2}Mn_{0.8}Co_{0.2}O_3$ in the spin-up and spin-down states, (b–f) calculated partial density of states (PDOS) in the spin-up and spin-down states for atom La, atom Sr, atom Mn, atom Co, and atom O, respectively.

4.2 Optical properties

Owing to the rhombohedral symmetry of the $La_{0.8}Sr_{0.2}Mn_{0.8}Co_{0.2}O_3$ system, the optical responses along the *XX* and *YY* directions are identical; therefore, only the *XX* and *ZZ* components are considered. The real and imaginary parts of the dielectric function were analyzed, in the field of linear optics, using the relation of the Kramers–Kronig defined as:[21]

$$\varepsilon(\omega) = \varepsilon_1(\omega) + i\varepsilon_2(\omega) \quad (5)$$

The dielectric function is derived from interband transitions between occupied and unoccupied electronic states, as obtained from density functional theory calculations,[22] a methodology widely used for previous perovskite compounds.[23]

The complex dielectric function is directly related to the complex refractive index:[24]

$$\tilde{n} = n + ik \quad (6)$$

where n is the refractive index and k is the extinction coefficient.

The relation between the quantities is expressed as $\varepsilon_1 = n^2 - k^2$ and $\varepsilon_2 = 2nk$, where $\varepsilon_1(\omega)$ describes the dispersion of the electromagnetic radiation after interaction with the surface of the material and therefore the polarization of light, while $\varepsilon_2(\omega)$ accounts for the absorption of electromagnetic radiation incident on the material.[25]

Important optical constants, such as the refractive index, $n(\omega)$, the extinction coefficient, $k(\omega)$, and the real part of optical conductivity, Re$[\sigma(\omega)]$, are directly related to $\varepsilon_1(\omega)$and $\varepsilon_2(\omega)$ through the Kramers–Kronig relations, providing a complete description of the material's optical response.[21,26]

$$n(\omega) = \left(1/\sqrt{2}\right) \times \left[\sqrt{\varepsilon_1(\omega)^2 + \varepsilon_2(\omega)^2} + \varepsilon_1(\omega)\right]^{1/2} \quad (7)$$

$$k(\omega) = \left(1/\sqrt{2}\right) \times \left[\sqrt{\varepsilon_1(\omega)^2 + \varepsilon_2(\omega)^2} - \varepsilon_1(\omega)\right]^{1/2} \quad (8)$$

$$\text{Re}\ \sigma(\omega) = \frac{\omega\varepsilon_2(\omega)}{4\Pi} \quad (9)$$

During the calculations, a Lorentzian interband broadening parameter (Γ) of 0.1 eV was applied to account for the finite lifetime of the excited states and to produce smooth optical spectra without excessive smearing. The Drude damping parameter was set to 0.2 eV, chosen consistently with the interband broadening to ensure a physically coherent description of the low-energy intraband optical response.

The real part ε_1, shown in Fig. 4a, exhibits a high static dielectric constant $\varepsilon_1(0)$, highlighting the low-frequency polarizability. This behaviour originates from the significant hybridization between O 2p and transition-metal (Mn/Co) 3d orbitals, which enhances the electronic delocalization, a characteristic feature of perovskite oxide materials.[27,28] A sharp drop in ε_1 is observed, crossing zero and becoming negative around 0.803 eV, reaching a local minimum indicative of plasma

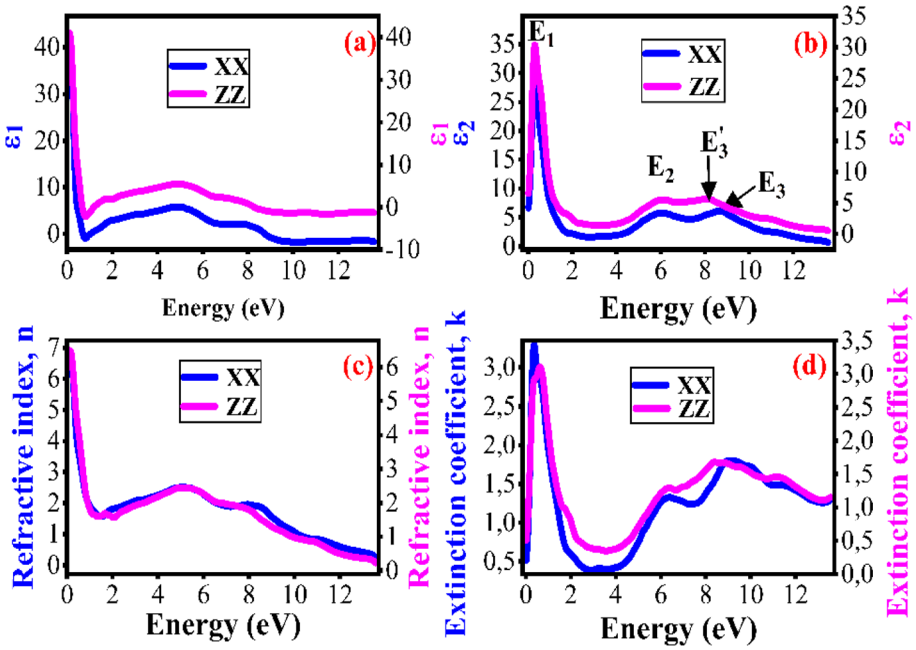

Fig. 4 Directional optical properties along the *XX* and *ZZ* directions of $La_{0.8}Sr_{0.2}Mn_{0.8}Co_{0.2}O_3$: (a) real part of the dielectric constant, (b) imaginary part of the dielectric constant, (c) refractive index, and (d) extinction coefficient.

frequency. Beyond this point, ε_1 increases to 4.884 eV before gradually decreasing and becoming negative at around 8.776 eV, pointing to a strong reflectivity typical of optical metals.[29,30]

The imaginary part ε_2, presented in Fig. 4b, representing the optical absorption of our sample, shows distinct peaks E_1, E_2, E_3 and $E_3^{'}$. The prominent low-energy peak E_1, around 0.286 eV, arises from transitions between partially occupied Mn/Co 3d states near the Fermi level, consistent with the metallic behaviour inferred from the electronic density of states. The other three peaks E_2, E_3 and $E_3^{'}$, observed near 6 eV, 8.149 eV and 8.667 eV, respectively, correspond to higher energy transitions

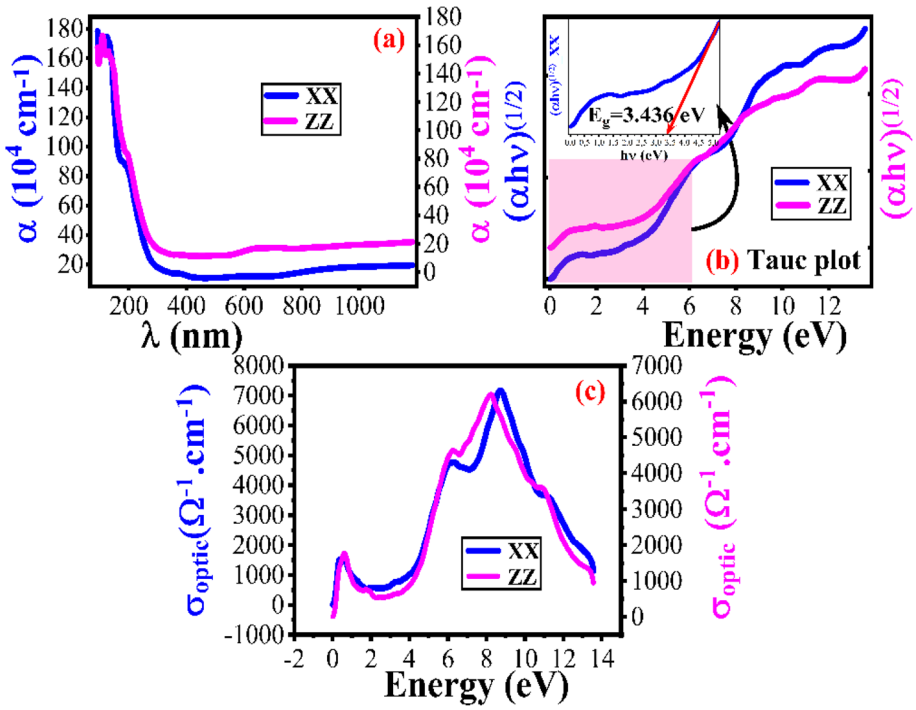

Fig. 5 Calculated optical properties of $La_{0.8}Sr_{0.2}Mn_{0.8}Co_{0.2}O_3$: (a) absorption coefficient, (b) Tauc plot for band gap determination, inset shows the linear extrapolation of the Tauc plot used to estimate the optical band gap, and (c) optical conductivity.

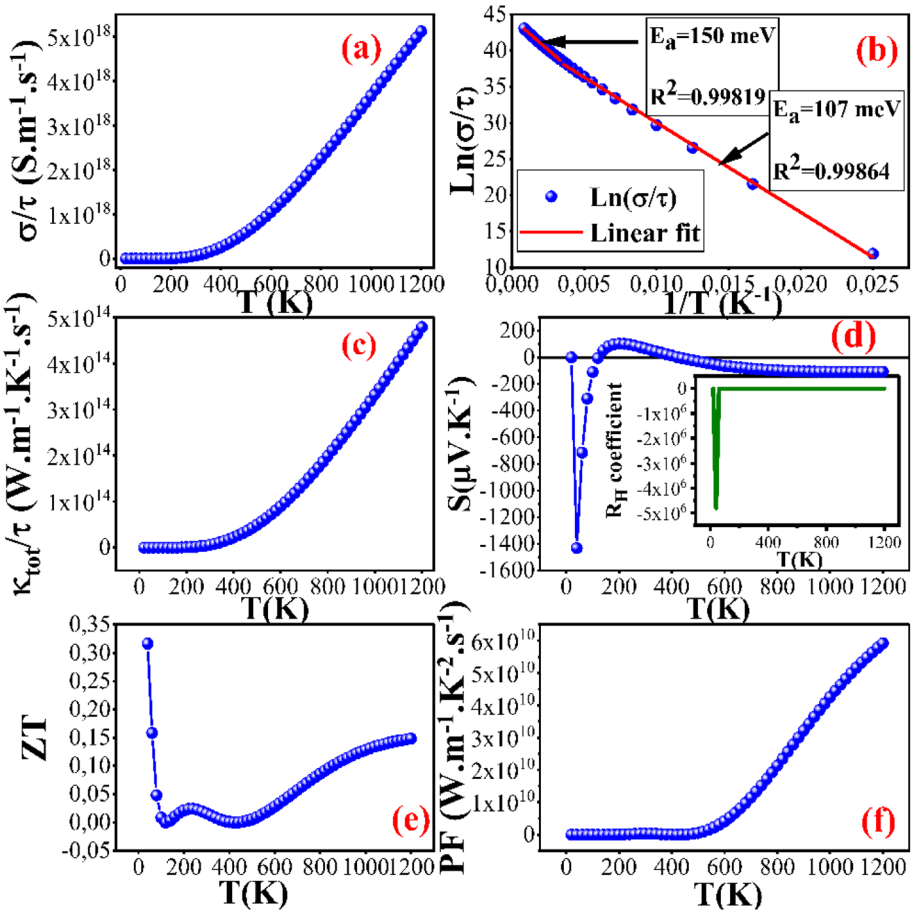

Fig. 6 Calculated thermoelectric properties of $La_{0.8}Sr_{0.2}Mn_{0.8}Co_{0.2}O_3$: (a) electrical conductivity per relaxation time σ/τ, (b) determination of activation energy E_a using the Arrhenius relation, (c) total thermal conductivity per relaxation time κ_{tot}/τ, (d) the Seebeck coefficient S, with an inset showing the Hall coefficient, (e) the dimensionless figure of merit ZT and (f) the power factor PF.

from deeper valence states to the conduction band.[31] The progressive decrease of ε_2 beyond ~9 eV indicates a reduction in optical absorption and a subsequent trend to an optical transparency regime.

These observations are mirrored in the behaviour of the refractive index n, as shown in Fig. 4c, which reaches a sharp maximum of approximately 6.5 around 0.15 eV for both *XX* and *ZZ* directions, reflecting strong electronic polarizability and a high density of states near the Fermi level. Then, n decreases rapidly after this peak below 2 eV, which indicates the start of strong optical absorption. Between 2 and 8.5 eV, n shows a secondary broad maximum typically arising from multiple overlapping interband transitions, involving deeper electronic states. Beyond 10 eV, the refractive index steadily decreases, indicating reduced absorption and an evolution towards an optical transparency regime.[32]

The extinction coefficient k, presented in Fig. 4d, further confirms these features, exhibiting a strong absorption peak near 0.367 eV (*XX* direction), which is in agreement with the low-energy peak observed in ε_2. Additional peaks at 6.408 eV, 9.265 eV and 11.388 eV were observed, attributed to higher energy interband transitions.[32] The gradual decrease in k beyond 11.5 eV supports the start of a transparency regime at high photon energies. Overall, the moderate but persistent difference in anisotropy observed for ε, n, and k across the energy spectrum confirms a directionally dependent optical response due to structural distortions.

The absorption coefficient α was computed from the complex dielectric function through the following relation:[33]

$$\alpha(\omega) = \frac{\sqrt{2}\omega}{C}\left[\sqrt{\varepsilon_1^2(\omega) + \varepsilon_2^2(\omega)} - \varepsilon_1(\omega)\right]^{1/2} \quad (10)$$

The frequency-dependent optical response is essential for evaluating the performance of the material in optoelectronic applications.[34] Fig. 5a displays the absorption coefficient α as a function of wavelength λ along the *XX* and *ZZ* directions. A pronounced increase is observed in the ultraviolet region below 300 nm, reflecting strong absorption in this spectral range.

Fig. 5b presents the Tauc plot in which $(\alpha h\nu)^{1/2}$ is plotted as a function of photon energy $(h\nu)$, for materials with indirect allowed transitions,[35] following the relation:

$$(\alpha h\vartheta)^{1/2} = C \times (h\vartheta - E_g) \quad (11)$$

where C is a constant, $h\vartheta$ is the photon energy, and E_g is the band gap energy.

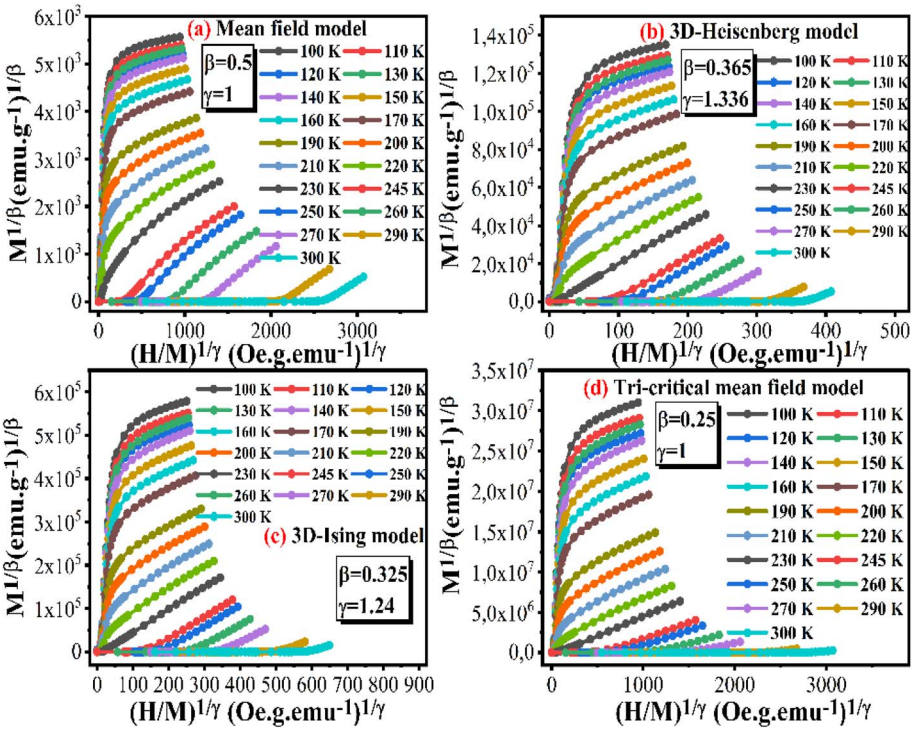

Fig. 7 Modified Arrott plots $M^{1/\beta}$ *vs.* $(H/M)^{1/\gamma}$ for LS1 based on different models: (a) mean field model, (b) 3D Heisenberg model, (c) 3D Ising model and (d) tri-critical mean-field model.

From the linear extrapolation of the absorption plot to the energy axis, the energy gap is estimated to be approximately 3.436 eV, which is consistent with the value obtained from the electronic band structure graph (Fig. 1).

Fig. 5c shows the real part of the optical conductivity as a function of photon energy, revealing four distinct peaks located at approximately 0.6 eV, 6.3 eV, 8.7 eV and 11 eV. These peaks are attributed to interband transitions from occupied to unoccupied electronic states. Notably, the optical conductivity

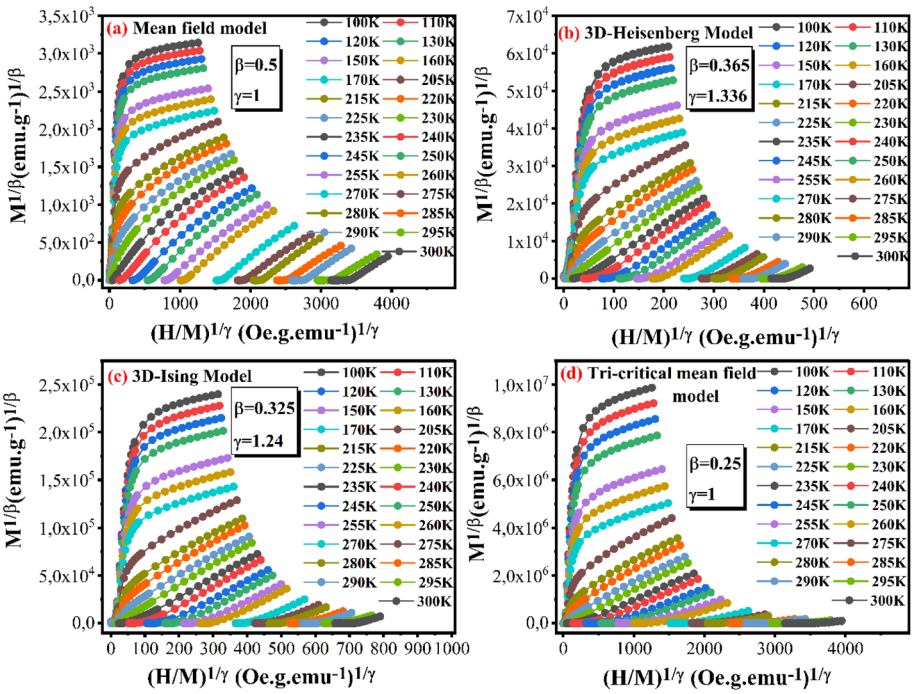

Fig. 8 Modified Arrott plots $M^{1/\beta}$ *vs.* $(H/M)^{1/\gamma}$ for LS2 based on different models: (a) mean field model, (b) 3D Heisenberg model, (c) 3D Ising model and (d) tri-critical mean-field model.

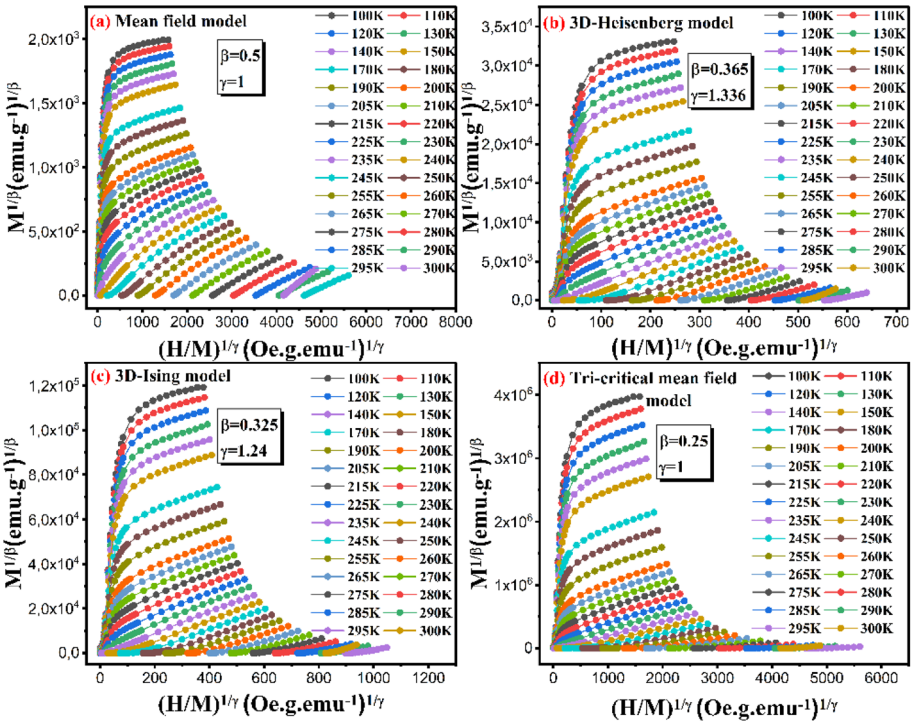

Fig. 9 Modified Arrott plots $M^{1/\beta}$ *vs.* $(H/M)^{1/\gamma}$ for LS3 based on different models: (a) mean field model, (b) 3D Heisenberg model, (c) 3D Ising model and (d) tri-critical mean-field model.

of our sample increases significantly in the ultraviolet region, which is in agreement with the strong absorption observed in this range.

4.3 Thermoelectric properties

The transport properties can be derived from the band structure using semi-classical Boltzmann transport theory.[36]

Fig. 6a illustrates the temperature dependence of the electrical conductivity per relaxation time, σ/τ, displaying negligible change at lower temperatures, suggesting minimal thermal activation of charge carriers. This phenomenon may be associated with the limited mobility of charge carriers.

A pronounced rise in electrical conductivity per relaxation time is observed with increasing temperature, driven by the enhanced mobility of thermally activated charge carriers, suggesting a semiconducting behaviour. At room temperature, the electrical conductivity per relaxation time reaches approximately 7.091×10^{16} S m^{-1} s^{-1}, which lies within the range reported for oxide perovskite, such as 3.44×10^{19} S m^{-1} s^{-1}, reported for $Ba_{0.85}S_{0.15}Ti_{0.85}Zr_{0.15}O_3$,[37] and 8.56×10^{18} S m^{-1} s^{-1} for $NaNbO_3$.[38]

The temperature dependence of electrical conductivity per relaxation time was further analyzed through the $\mathrm{Ln}(\sigma/\tau)$ *vs.* $1/T$ plot, shown in Fig. 6b. Two distinct linear regions were identified, indicating a change in the dominant conduction mechanism. In the low-temperature region ($T < 300$ K), the extracted activation energy is approximately 107 meV, while in the high-temperature region ($T > 300$ K), the value increased to 150 meV. This change may indicate a possible crossover from small polaron hopping at low temperatures to thermally activated band conduction at elevated temperatures, consistent with previous reports on manganite systems.[39,40]

The thermal conductivity per relaxation time κ_{tot}/τ of $La_{0.8}Sr_{0.2}Mn_{0.8}Co_{0.2}O_3$, depicted in Fig. 6c, follows a similar trend to that of electrical conductivity per relaxation time, which is qualitatively consistent with the Wiedemann–Franz law ($\kappa = \sigma \times L \times T$, where L denotes the Lorentz number).[41] It remains nearly constant at low temperatures and then increases significantly at higher temperatures. At room temperature, the thermal conductivity per relaxation time is approximately 6.21×10^{12} W m^{-1} K^{-1} s^{-1}, which is consistent with the range of values reported for oxide perovskites.[37,38]

Fig. 6d displays the variation of the Seebeck coefficient (S) with temperature. Between 20 K and 120 K, S exhibits large negative values, indicating n-type conduction dominated by electrons, which is supported by the negative sign of the Hall coefficient presented in the inset of Fig. 6d. This regime is often associated with small polaron hopping, commonly observed in mixed-valence perovskite oxides such as $La_{1-x}Sr_xCoO_3$ and $La_{1-x}Ca_xMnO_3$.[42,43]

With increasing temperature, S undergoes a sign reversal, attaining positive values between 140 K and 420 K, which implies a transition from n-type to p-type conduction. Despite this sign inversion in $S(T)$, the Hall coefficient remains negative across the entire temperature range, which may indicate that electrons remain the dominant carriers, while holes contribute as minority carriers, a behaviour previously reported in related cobaltite systems undergoing spin-state or carrier type transitions.[43,44]

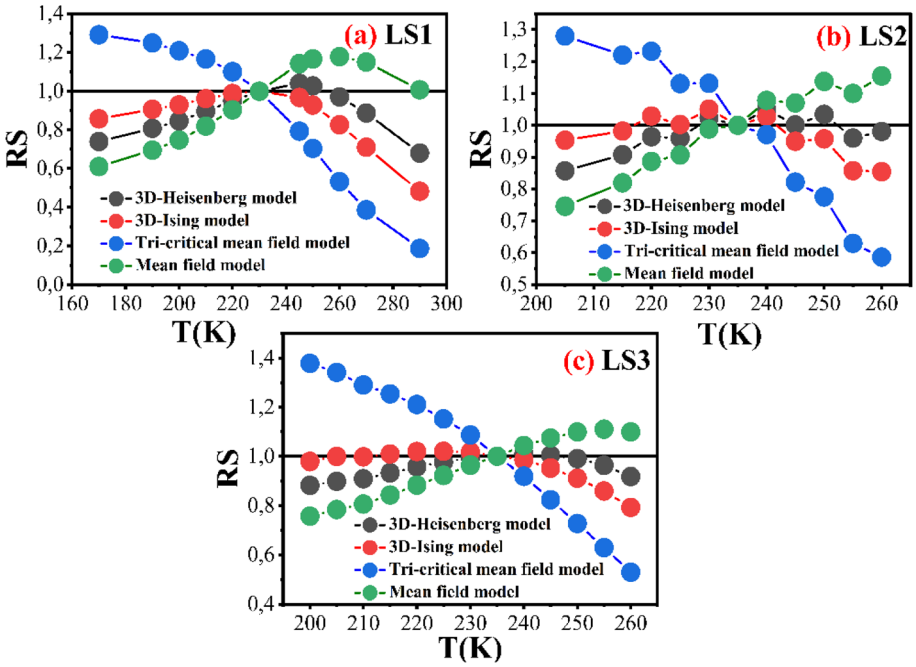

Fig. 10 Variation of relative slope RS as a function of temperature for (a) LS1, (b) LS2 and (c) LS3 samples.

Above 440 K, S gradually decreases and becomes negative again, confirming the re-establishment of n-type conduction at high temperatures. At room temperature, S reaches a value of approximately 67.673 μV K^{-1}.

The dimensionless figure of merit $ZT = \frac{S^2\sigma T}{k}$, which evaluates the efficiency of energy conversion in thermoelectric materials, is depicted in Fig. 8e. The curve displays a monotonic behaviour, with a sharp initial peak of approximately 0.32 at 40 K, followed by a significant drop to a minimum at 120 K and then a gradual increase with temperature, reaching 0.15 at 1200 K. This upward trend correlates with the increase in power factor (Fig. 8f) and the thermal conductivity per relaxation time (Fig. 6c), which is consistent with previous reports on doped perovskites, where increased carrier mobility and spin-state transitions contribute to thermoelectric enhancement.[45,46] Furthermore, the activation energy derived from the Arrhenius plot (Fig. 6b) indicates thermally activated transport, suggesting a potential improvement in thermoelectric performance at higher temperatures.[47]

The evolution of the power factor (PF) as a function of temperature, defined as $PF = S^2 \times \frac{\sigma}{\tau}$, is depicted in Fig. 6f. The PF shows a gradual increase with temperature, reaching a value of 5.92×10^{10} W m^{-1} K^{-2} s^{-1} at 1200 K.

4.4 Critical exponents and scaling analysis

4.4.1 Modified Arrott plots method. Arrott plots assume that the critical exponents adhere to mean field theory, where the critical exponents for spontaneous magnetization, $M_S(T)$, and inverse magnetic susceptibility, $\chi_0^{-1}(T)$, are typically 0.5 and 1, respectively.[48]

For systems with long-range ferromagnetic interactions, the Arrott plots appear as straight lines parallel to each other in the immediate vicinity of the Curie temperature.

Thus, in this method, M_S and χ_0^{-1} are defined as the points where the linear segments of the isotherms intersect the M^2 (for $T < T_C$) and H/M (for $T > T_C$) axes, respectively, and the Curie temperature corresponds to the Arrott plot passing through the origin.

The Arrott plots of the three samples shown in Fig. 7–9 do not show a series of parallel lines, as expected for long-range ferromagnetic order. In contrast, they exhibit non-linear behaviour, indicating the presence of short-range magnetic correlations. This suggests that the critical exponents of the mean-field model are not suitable for these samples.

To identify the most accurate model describing the phase transition of the samples, the Arrott–Noakes equation, given by the following formula, is used:[49]

$$(H/M)^{1/\gamma} = a \times \varepsilon + b \times M^{1/\beta} \quad (12)$$

where $\varepsilon = (T - T_C)/T_C$ is the reduced temperature, a and b are constants.

Modified Arrott plots, also known as Arrott–Noakes plots, are a graphical technique used to study the magnetic properties of materials, in particular to analyse magnetic phase transitions, and accurately determine critical exponents.

To construct modified Arrott plots, three types of exponents associated with the following models are used: the 3D Heisenberg model (with $\beta = 0.365$ and $\gamma = 1.336$), the 3D Ising model (with $\beta = 0.325$ and $\gamma = 1.24$), and the mean-field critical model (with $\beta = 0.25$ and $\gamma = 1$).[50]

As depicted in Fig. 7–9, all the curves show an almost linear behaviour within the high-magnetic-field region.

The relative slope RS, defined as $RS = S(T)/S(T_C)$,[51] can be used to evaluate and compare the models used to identify the most appropriate one for each of LS1, LS2 and LS3 compounds, as shown in Fig. 10. For the most appropriate model, it is desirable that RS is close to one.

All RS values, except for those of the mean-field critical model, appear to be close to one. This suggests that the other three models may provide better descriptions of magnetic critical exponents. However, at this stage, the best model for the three compounds remains uncertain. A precise iterative method[52] was used to confidently select the most appropriate model and determine the critical exponents β and γ. This method involved linear extrapolation of the isotherms in the high-magnetic-field region. This extrapolation allowed the derivation of values for $M_S(T)$ and $\chi_0{-}1(T)$, which represent the intersections of the extrapolated isotherms with the $M^{1/\beta}$ and $(H/M)^{1/\gamma}$, respectively.

Fitting the data with eqn (13) and (14) gives initial values of β and γ. These initial values were then used to reconstruct a modified Arrott plot. New values for $M_S(T)$ and $\chi_0{}^{-1}(T)$ are then derived by linear extrapolation of the high-field region. Additional β and γ values are then generated iteratively. This process continues until the β and γ values converge to stability, indicating optimal values for these critical exponents, as shown in Fig. 11a–c.

$$M_S(T) = M_S(0) \times (-\varepsilon)^{\beta}, \text{ for } T < T_C, \varepsilon < 0 \quad (13)$$

$$\chi_0{}^{-1}(T) = \chi_0{}^{-1}(0) \times \varepsilon^{\gamma}, \text{ for } T > T_C, \varepsilon > 0 \quad (14)$$

4.4.2 Kouvel–Fisher method. The critical exponents previously deduced from the MAP method can be accurately determined using the Kouvel–Fisher method,[53] based on the following equations:

$$M_S(T)/(dM_S(T)/dT) = (T - T_C)/\beta \quad (15)$$

$$\chi_0{}^{-1}(T)/(d\chi_0{}^{-1}(T)/dT) = (T - T_C)/\gamma \quad (16)$$

These equations suggest that $M_S(T)/(dM_S(T)/dT)$ and $\chi_0{}^{-1}(T)/(d\chi_0{}^{-1}(T)/dT)$ are temperature-dependent functions whose plots are straight lines. The slopes of these functions are $1/\beta$ and $1/\gamma$, respectively.

T_C is identified as the intersection of the lines with the temperature axes. As depicted in Fig. 12a–c, linear fits provide the values of β at T_C and γ at T_C.

In accordance with Widom's scaling law,[54] $\delta = 1 + \gamma/\beta$, the critical exponent δ can be derived using the previously determined values from both the MAP and the Kouvel–Fisher methods. Table 2 shows the values of the three exponents.

Based on the results presented in Table 2, for the LS1 sample, the β values derived from MAP and Kouvel–Fisher methods are closer to that of the 3D Heisenberg model (0.365), while the γ values are closer to that of the 3D Ising model (1.24). This suggests the presence of short-range ferromagnetic interactions between the nanoparticles of LS1.

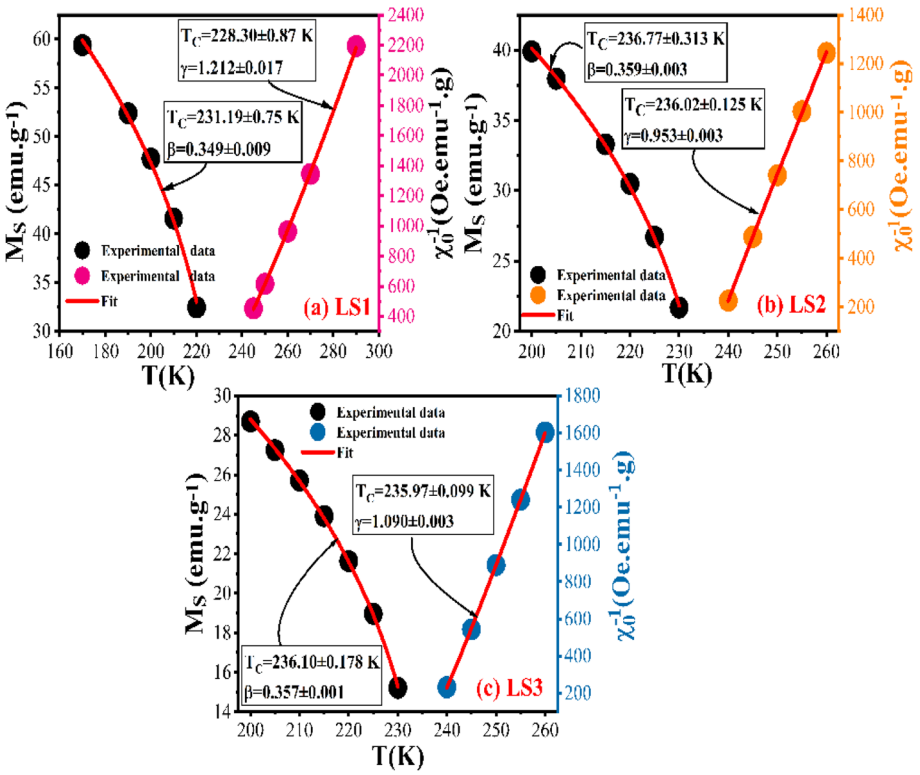

Fig. 11 Temperature dependence of spontaneous magnetization $M_S(T)$ (left) and inverse initial susceptibility $\chi_0{}^{-1}(T)$ (right) with fitting curves for (a) LS1, (b) LS2 and (c) LS3 samples.

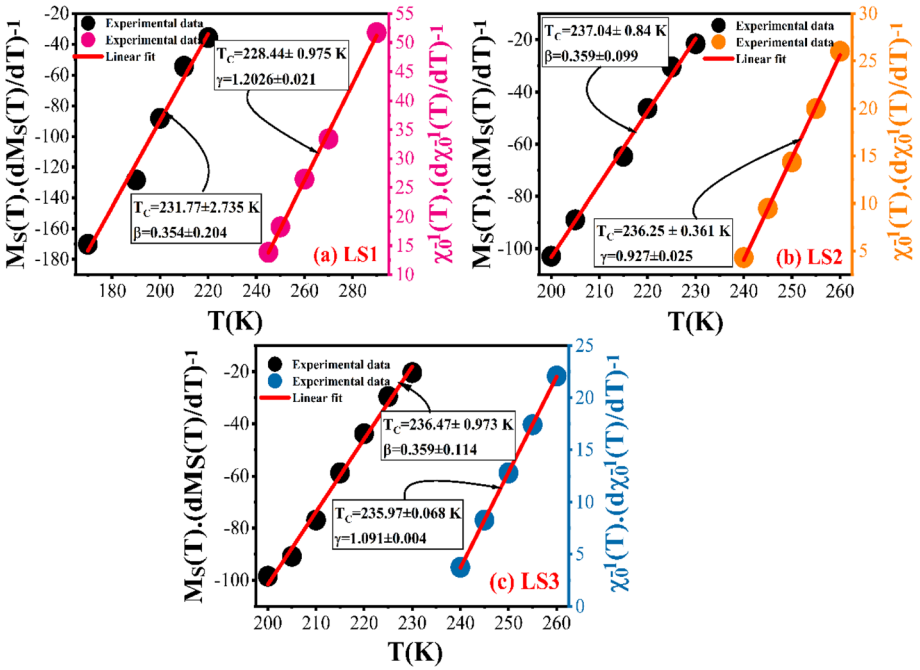

Fig. 12 Kouvel–Fisher plots of $M_S(T)/(dM_S(T)/dT)$ (left) and $\chi_0^{-1}(T)/(d\chi_0^{-1}(T)/dT)$ (right) with fitting curves for (a) LS1, (b) LS2, and (c) LS3 samples.

Table 2 Comparison of the critical exponents of samples LS1, LS2 and LS3 with the different theoretical models

Model/sample	Ref.	Method	β	γ	δ
Mean field model	55	Theory	0.5	1	3
3D Heisenberg model	55	Theory	0.365	1.336	4.80
3D ising model	55	Theory	0.325	1.24	4.82
Tri-critical mean field model	55	Theory	0.25	1	5
LS1 sample	This work	MAP	0.349	1.212	4.473
		KF	0.354	1.2026	4.397
		CI	—	—	4.59
LS2 sample	This work	MAP	0.359	0.953	3.655
		KF	0.359	0.927	3.582
		CI	—	—	3.90
LS3 sample	This work	MAP	0.357	1.090	4.053
		KF	0.359	1.091	4.038
		CI	—	—	4.66

For LS2 and LS3 samples, the β values derived from the MAP and Kouvel–Fisher methods are closer to that of the 3D Heisenberg model (0.365), as for LS1. However, the γ values for both samples are closer to that of the mean-field model,[56] suggesting the presence of both long- and short-range interactions between the nanoparticles of LS2 and LS3 samples. This could be attributed to the coexistence of ferromagnetic interactions *via* double exchange and antiferromagnetic interactions *via* superexchange, as well as the presence of magnetic inhomogeneities.

4.4.3 The critical isotherm method. The third critical exponent, δ, is determined by fitting the critical magnetization isotherm curve to the applied magnetic field using the following equation:[57]

$$M = D \times H^{1/\delta}, \text{ for } T = T_C, \varepsilon = 0 \quad (17)$$

For greater accuracy, the value of δ can also be obtained by linearly fitting $\ln(M)$ *vs.* $\ln(H)$, where the slope of this curve is equal to $1/\delta$.

Fig. 13 illustrates the log–log scale of the isothermal magnetization $M(H)$ at T_C.

From the results presented in Table 2, it can be seen that the critical exponent δ, determined from the critical isotherm, is in close agreement with the values obtained from the MAP and Kouvel–Fisher methods.

4.4.4 Validity of the critical exponents. A scaling analysis can also confirm the validity of the critical exponents and the obtained Curie temperatures T_C. Fig. 14 was plotted according to the following equation:[58]

$$M(H,\varepsilon) = \varepsilon^{\beta} f_{\pm}(H/\varepsilon^{\gamma+\beta}) \quad (18)$$

where f_- for $T < T_C$ and f_+ for $T > T_C$ are regular functions.

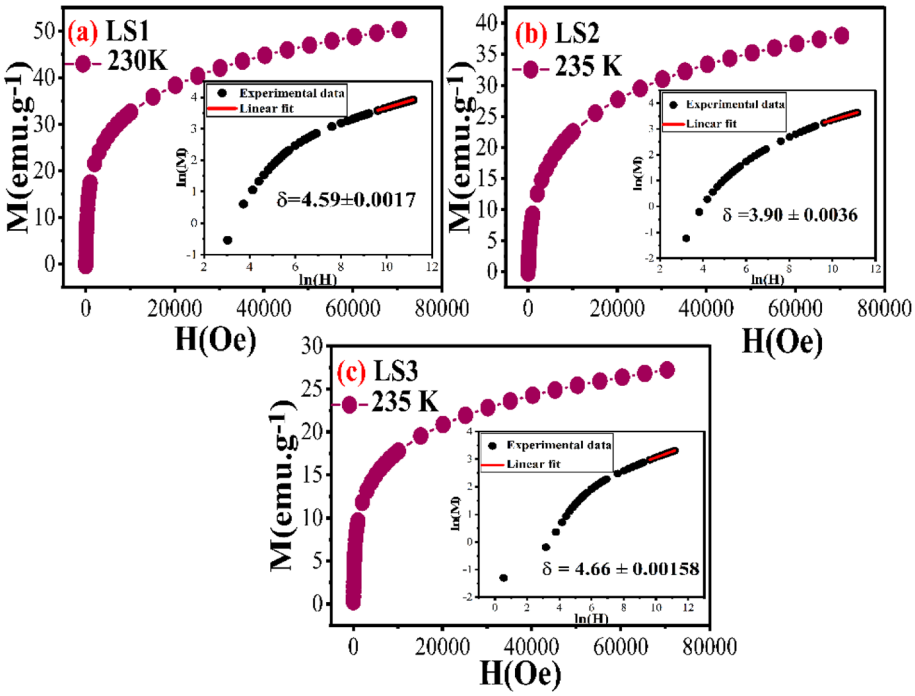

Fig. 13 Isothermal magnetization curves at T_C for samples (a) LS1, (b) LS2 and (c) LS3. The insets show the determination of the critical exponent δ from ln(M) *vs.* ln(H) curve at T_C.

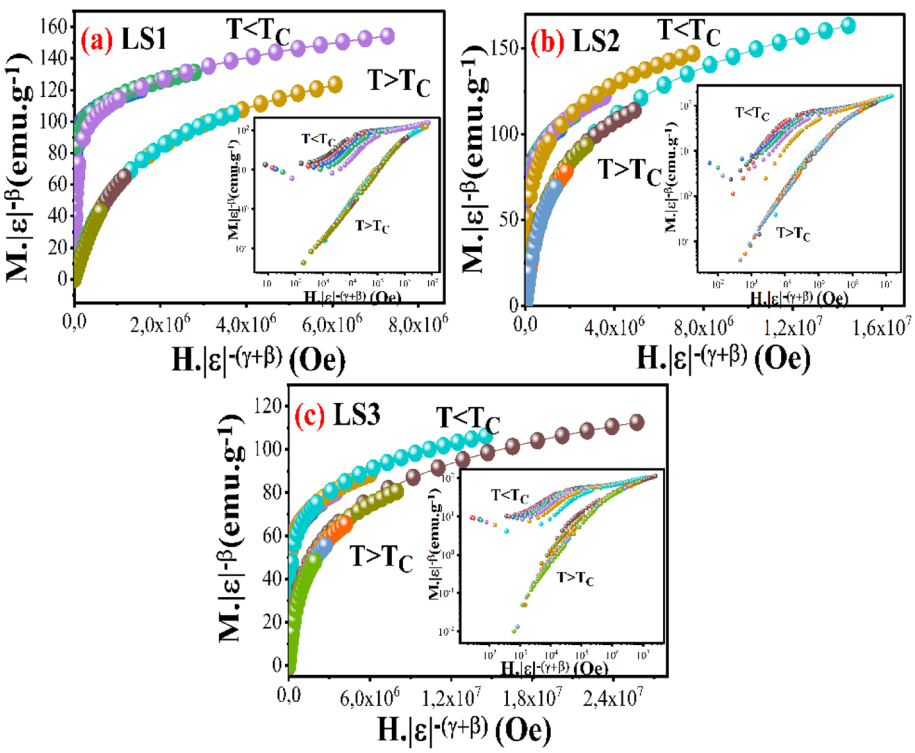

Fig. 14 Scale diagrams showing two universal curves below and above T_C for (a) LS1, (b) LS2 and (c) LS3 samples. Insets display the same curves on the log–log scale.

Fig. 14 shows the variation of $M \times |\varepsilon|^{-\beta}$ *vs.* $H \times |\varepsilon|^{-(\beta+\gamma)}$ over the temperature range around T_C using β, γ and T_C values obtained from the Kouvel–Fisher method.

By applying a logarithmic scale (shown in the inset of Fig. 14), two distinct branches were observed, one for temperatures below T_C and a second for temperatures above T_C.

These universal curves validate the adherence to the scaling hypothesis, affirming the significance of the critical exponent values obtained in delineating the suitable model for the samples.

5 Conclusion

The results of DFT calculations demonstrated that $La_{0.8}Sr_{0.2}Mn_{0.8}Co_{0.2}O_3$ exhibited spin-dependent transport with a p-type semiconducting behaviour in one configuration and a metallic behaviour in the other. Optical analysis confirmed its high dielectric response and ultraviolet absorption. Thermoelectric investigations demonstrated a thermally activated carrier transport and a strong power factor at high temperatures. Critical exponent analysis revealed distinct magnetic behaviours, where LS1 exhibited short-range magnetic behaviour, consistent with the 3D Heisenberg model, while LS2 and LS3 showed mixed short- and long-range interactions.

Author contributions

L. Karoui: writing, methodology, conceptualization, data curation, writing-original draft. A. Mabrouki: DFT calculations, validation. T. Mnasri: supervision, editing, validation. M. Smari: SEM characterization, validation. A. Bajorek: M-H isothermal magnetization measurements, validation. All authors reviewed and approved the final version of the manuscript.

Conflicts of interest

There are no conflicts to declare.

Data availability

All data supporting the findings of this study are included within the main article.

Acknowledgements

The magnetic measurements were performed with funding from the statutory subsidies for research activities of the Condensed Phase Research Team in the A. Chelkowski Institute of Physics, University of Silesia in Katowice, Poland.

References

1 G. B. Goodenough, Theory of the role of covalence in the perovskite type manganites [La, M(II)]MnO_3, *Phys. Rev.*, 1955, **100**, 564–573.
2 Y. Tokura, Critical features of colossal magnetoresistive manganites, *Rep. Prog. Phys.*, 2006, **69**, 797.
3 M. B. Salamon and M. Jaime, The physics of manganites: structure and transport, *Rev. Mod. Phys.*, 2001, **73**, 583.
4 P. M. Raccah and J. B. Goodenough, First-order localized-electron collective-electron transition in $LaCoO_3$, *Phys. Rev.*, 1967, **155**, 932–943.
5 M. A. Korotin, *et al.*, Intermediate-spin state and properties of $LaCoO_3$, *Phys. Rev. B: Condens. Matter Mater. Phys.*, 1996, **54**, 5309.
6 L. Karoui, M. Smari, T. Mnasri and A. Bajorek, Correction: The effect of the gelation temperature on the structural, magnetic and magnetocaloric properties of perovskite nanoparticles manufactured using the sol-gel method, *RSC Adv.*, 2024, **14**, 19983.
7 E. A. Kotomin, E. A. Evarestov, Y. A. Mastrikov and J. Maier, DFT plane wave calculations of the atomic and electronic structure of $LaMnO_3$ (001) surface, *Phys. Chem. Chem. Phys.*, 2005, **7**, 2346–2350.
8 J. He and C. Franchini, Screened hybrid functional applied to $3d^0 \rightarrow 3d^8$ transition-metal perovskites $LaMO_3$ (M= Sc-Cu): Influence of the exchange mixing parameter on the structural, electronic, and magnetic properties, *Phys. Rev. B: Condens. Matter Mater. Phys.*, 2012, **86**, 235117.
9 Y. Wang and H. P. Cheng, Oxygen reduction activity on perovskite oxide surfaces: a comparative first principle study of $LaMnO_3$, La FeO_3 and $LaCrO_3$, *J. Phys. Chem. C*, 2013, **117**, 2106–2112.
10 J. H. Lee and B. Kim, Revisiting LaMnO3: A density functional theory study, *Curr. Appl. Phys.*, 2025, **78**, 7–14.
11 D. Shi, M. Ye, L. Zhao, *et al.*, Critical properties of perovskite manganite $La_{0.88}Sr_{0.12}MnO_3$ nanocrystalline, *J. Sol-Gel Sci. Technol.*, 2023, **107**, 725–732.
12 D. Turki, Z. K. Ghouri, S. Al-Meer, K. Elsaid, M. I. Ahmad, A. Easa, G. Remenyi, S. Mahmood, E. Hlil, M. Ellouze and F. Elhalouani, Critical behavior of $La_{0.8}Ca_{0.2}Mn_{1-x}Co_xO_3$ perovskite ($0.1 \leq x \leq 0.3$), *Magnetochemistry*, 2017, **3**, 28.
13 M. H. Phan, *et al.*, Tricritical point and critical exponents of $La_{0.7}Ca_{0.3-x}Sr_xMnO_3$ (x= 0, 0.05, 0.1, 0.2, 0.25) single crystals, *J. Alloys Compd.*, 2010, **508**, 238–244.
14 S. Bouzidi, M. Dhahri, J. Dhahri and E. K. Hlil, Universal critical behavior in polycrisalline $La_{0.75}Ca_{0.25-x}Na_xMnO_3$ (x= 0, 0.05) samples, *Eur. Phys. J. Plus*, 2021, **136**, 23.
15 G. K. H. Madsen and D. J. Singh, BoltzTrap. A code for calculating band-structure dependent quantities, *Comput. Phys. Commun.*, 2006, **175**, 67–71.
16 A. Mabrouki, O. Messoudi, M. Mansouri, S. Elgharbi and A. Bardaoui, Study of the structural, electronic, magnetic and magnetocaloric properties of $La_{0.5}Ca_{0.5}Mn_{0.9}V_{0.1}O_3$ sample: first principles calculation (DFT-MFT), *RSC Adv.*, 2021, **11**, 37896–37903.
17 A. Mabrouki, A. Bougoffa, T. Mnasri, A. Benali, E. Dhahri and M. A. Valente, Narrow band gap in $La_{0.8}MnO_{2.8}$ as a new promising solar cell absorber, *AMMS*, 2021, **6**, 000648.
18 U. Qazi, S. Mehmood, Z. Ali, I. Khan and I. Ahmad, Electronic structure and magnetic properties of the perovskites $SrTMO_3$ (TM= Mn, Fe, Co, Tc, Ru, Rh, Re, Os and Ir), *Phys. B*, 2022, **624**, 413361.
19 J. Kanamori, Crystal distortion in magnetic compounds, *J. Appl. Phys.*, 1960, **31**, S14–S23.
20 M. M. S. H. Elkhalig and A. El-Taher, Study of structural, electronic and magnetic properties of transition-metalperovskite oxides $SrMO_3$ (M=Mn and Co) by XRD

and DFT techniques, *Dig. J. Nanomater. Biostruct.*, 2016, **11**, 1383–1396.

21 S. A. Dar, R. Sharma, V. Srivastava and U. K. Sakalle, Investigation on the electronic structure, optical, elastic, mechanical, thermodynamic and thermoelectric properties of wide band gap semiconductor double perovskite Ba_2InTaO_6, *RSC Adv.*, 2019, **9**, 9522–9532.

22 M. Gajdoš, K. Hummer, G. Kresse, J. Furthmüller and F. Bechstedt, Linear optical properties in the projector-augmented wave methodology, *Phys. Rev. B: Condens. Matter Mater. Phys.*, 2006, **73**, 045112.

23 H. Huang, W. Wang, L. Chen, H. Guan and Z. Xu, First-principles investigation of the electronic structure and magnetism in double perovskite $SrCaNiTeO_6$, *Mod. Phys. Lett. B*, 2026, **40**, 2650077.

24 P. Schygulla, *et al.*, Determination of the complex refractive index of compound semiconductor alloys for optical device modelling, *J. Phys. D: Appl. Phys.*, 2020, **53**, 495104.

25 A. Mabrouki, T. Mnasri, A. Bougoffa, A. Benali, E. Dhahri and M. A. Valente, Experimental study and DFT calculation of the oxygen deficiency effect on structural, magnetic and optical properties of $La_{0.8}MnO_{3-\delta}$ (δ=0, 0.1, and 0.2) compounds, *J. Alloys Compd.*, 2021, **860**, 157922.

26 D. G. Dadi, M. W. Shura and F. Gochole, DFT analysis of structural, electronic and optical properties of Ni and Zn doped CoS counter electrode for dye sensitized solar cells, *Sci. Rep.*, 2025, **15**, 35486.

27 J. Roberston, High dielectric constant oxides, *Eur. Phys. J. Appl. Phys.*, 2004, **28**, 265–291.

28 M. A. Peña and J. L. G. Fierro, Chemical structures and performance of perovskite oxides, *Chem. Rev.*, 2001, **101**, 1981–2017.

29 H. Ehrenreich and M. H. Cohen, Self-consistent field approach to the many-electron problem, *Phys. Rev.*, 1959, **115**, 786–790.

30 S. Lany and A. Zunger, Accurate prediction of defect properties in density functional supercell calculations, *Modell. Simul. Mater. Sci. Eng.*, 2009, **17**, 084002.

31 A. P. Sakhya, D. P. Rai, M. S. Sheikh, M. Mukherjee, A. Dutta and T. P. Sinha, Origin of the optical anisotropy and the electronic structure of Ru-based double perovskite oxides: DFT and XPS studies, *RSC Adv.*, 2017, **7**, 43531–43539.

32 K. Souifi, G. Raddaoui, M. Nasri, J. Khelif, E. Berdimurodov, M. DEMIR and K. Khirouni, Insights into structural, electronic, optical properties, and impedance spectroscopy of semi-doped perovskite $Nd_{0.5}Ba_{0.5}CoO_3$: a theoretical and experimental study, *Phys. B*, 2024, **674**, 415535.

33 J. N Hilfiker and T. Tiwald, Dielectric Function Modeling, in *Spectroscopic Ellipsometry for Photovoltaics: Fundamental Principles and Solar Cell Characterization*, ed. H. Fujiwara and R. Collins, Springer Ser. Opt. Sci., Springer, Cham, 2018, vol. 212, pp. 115–153.

34 H. Huang, W. Wang, J. Bi and B. Li, First-principles study of the electronic, mechanical, and optical properties of $AMn_{1-x}Fe_xO_3$ (A=La, Sr), *Mod. Phys. Lett. B*, 2026, **40**, 2650016.

35 V. Mursyalaat, V. I. Variani, W. O. S. Arsyad and M. Z. Firihu, The development of program for calculating the band gap energy of semiconductor material based on UV-Vis spectrum using delphi 7.0, *J. Phys. Conf.*, 2023, **2498**, 012042.

36 S. Yousuf, T. M. Bhat, S. Singh, Z. Saleem, S. A. Mir, S. A. Khandy, *et al.*, Applicability of semi-classical Boltzmann transport theory in understanding the thermoelectric properties of ZrNiSn and ZrNiPb half-heuslers, *AIP Conf. Proc.*, 2019, **2115**, 030420.

37 Y. Moualhi, A. Mabrouki, H. Rahmouni and E. Dhahri, Experimental optical analysis and DFT study of electronic, thermoelectric and optic characteristics of a Co-Doped perovskite system, *Mater. Adv.*, 2025, **6**, 9051–9063.

38 A. Mabrouki, A. Bougoffa, A. Trabelsi, E. Dhahri and K. Khirouni, Optical and thermoelectric properties of NaNbO3 thin film deposed by spray pyrolysis: Experimental and DFT study, *Eur. Phys. J. Plus*, 2022, **137**, 1–8.

39 D. Salazar, D. Arias, O. J. Durá and M. A. López de la Torre, Thermopower and electrical resistivity of $La_{1-x}Sr_xMnO_3$ (x=0.2, 0.3): Effect of nanostructure on small polaron transport, *J. Alloys Compd.*, 2014, **583**, 141–144.

40 A. Asamitsu, Y. Moritomo and Y. Tokura, Thermoelectric effect in $La_{1-x}Sr_xMnO_3$, *Phys. Rev. B: Condens. Matter Mater. Phys.*, 1996, **53**, R2952–R2955.

41 A. Kumara, D. Sivaprahsam and A. D. Thakur, Improvement of thermoelectric properties of Lanthanum cobaltate by Sr and Mn co-substitution, *J. Alloys Compd.*, 2018, **735**, 1787–1791.

42 J. Androulakis, P. Migiakis and J. Giapintzakis, $La_{0.95}Sr_{0.05}CoO_3$: an efficient room temperature thermoelectric oxide, *Appl. Phys. Lett.*, 2004, **84**, 1099–1101.

43 K. Berggold, M. Kriener, C. Zobel, A. Reichl, M. Reuther, R. Müller, A. Freimuth and T. Lorenz, Thermal conductivity, thermopower, and figure of merit of $La_{1-x}Sr_xCoO_3$, *Phys. Rev. B: Condens. Matter Mater. Phys.*, 2005, **72**, 155116.

44 M. Ohtaki, Recent aspects of oxide thermoelectric materials for power generation from mid to high temperature heat source, *J. Ceram. Soc. Jpn.*, 2011, **119**, 770–775.

45 S. Bhattacharya, S. Pal, A. Banerjee, H. D. Yang and B. K. Chaudhuri, Magnetotransport properties of alkali metal doped La-Ca-Mn-O system under pulsed magnetic field: Decrease of small polaron coupling constant and melting of polarons in the high temperature phase, *J. Chem. Phys.*, 2003, **119**, 3972.

46 X. Zhang and L. D. Zhao, Thermoelectric materials : Energy coversion between heat and electricity, *J. Materiomics*, 2015, **1**, 92–105.

47 A. Kumar, K. Kumari, B. Jayachandran, D. Sivaprahasam and A. D. Thakur, Thermoelectric properties of (1-x) $LaCoO_3$.x$La_{0.7}Sr_{0.3}MnO_3$ composite, *J. Alloys Compd.*, 2018, **749**, 1092–1097.

48 A. Arrott, Criterion for Ferromagnetism from Observations of Magnetic Isotherms, *Phys. Rev.*, 1957, **108**, 1394–1396.

49 A. Arrott and J. E. Noakes, Approximate equation of state for Nickel near its critical temperature, *Phys. Rev. Lett.*, 1967, **19**, 786.

50 S. N. Kaul, Static critical phenomena in ferromagnets with quenched disorder, *J. Magn. Magn. Mater.*, 1985, **53**, 5–53.

51 J. Phan, L. Ling, B. Hong, L. Zhang, L. Pi and Y. Zhang, Critical properties of the perovskite manganite La0.1Nd0.6Sr0.3Sr0.3MnO3, *Phys. Rev. B: Condens. Matter Mater. Phys.*, 2010, **81**, 144426.

52 A. K. Pramanik and A. Banerjee, Critical behavior at paramagnetic to ferromagnetic phase transition in $Pr_{0.5}Sr_{0.5}MnO_3$: A bulk magnetization study, *Phys. Rev. B: Condens. Matter Mater. Phys.*, 2009, **79**, 214426.

53 J. S. Kouvel and M. E. Fisher, Detailed Magnetic Behavior of Nickel Near its Curie Point, *Phys. Rev.*, 1964, **136**, A1626–A1632.

54 B. Widom, Equation of State in the Neighborhood of the Critical Point, *J. Chem. Phys.*, 1965, **43**, 3898–3905.

55 D. Kim, B. Revaz, B. L. Zink, F. Hellman, J. J. Rhyne and J. F. Mitchell, Tricritical Point and the Doping Dependence of the Order of the Ferromagnetic Phase Transition of $La_{1-x}Ca_xMnO_3$, *Phys. Rev. Lett.*, 2002, **89**, 227202.

56 J. Yang and Y. P. Lee, Critical behavior in Ti-doped manganites $LaMn_{1-x}Ti_xO_3$ ($0.05 \leq x \leq 0.2$), *Appl. Phys. Lett.*, 2007, **91**, 142512.

57 J. Khelifi, M. Nasri and E. Dhahri, Investigation of the critical magnetic properties in $La_{0.6}Sr_{0.4}Mn_{0.9}V_{0.1}O_3$ manganite oxide, *J. Supercond. Novel Magn.*, 2016, **29**, 753–758.

58 S. Biswas and S. Keshri, Large magnetocaloric effect near room temperature in $La_{0.67}(Sr, K/Pb)_{0.33}MnO_3$ manganite nanomaterials, *J. Mater. Sci. Mater. Electron.*, 2020, **31**, 21896–21912.